Laser Beam Propagation in Random Media

NEW AND ADVANCED TOPICS

Larry C. Andrews
Melissa K. Beason

SPIE PRESS
Bellingham, Washington USA

Library of Congress Cataloging-in-Publication Data

Names: Andrews, Larry C., author. | Beason, Melissa, author.
Title: Laser beam propagation in random media : new and advanced topics / Larry C. Andrews, Melissa Beason.
Description: Bellingham, Washington : SPIE, [2022] | Includes bibliographical references and index.
Identifiers: LCCN 2022026397 | ISBN 9781510656505 (paperback) | ISBN 9781510656499 (pdf)
Subjects: LCSH: Laser beams–Atmospheric effects. | Laser beams. | Atmospheric turbulence.
Classification: LCC QC976.L36 A634 2022 | DDC 621.36/6–dc23/eng/20220727
LC record available at https://lccn.loc.gov/2022026397

Published by
SPIE
P.O. Box 10
Bellingham, Washington 98227-0010 USA
Phone: +1 360.676.3290
Fax: +1 360.647.1445
Email: books@spie.org
Web: www.spie.org

Cover image credit: iStock / Getty Images Plus – bs_k1d
Printed in the United States of America.
First printing 2023.
For updates to this book, visit http://spie.org and type “PM354” in the search field.

SPIE.

Contents

Preface

This research monograph is a companion edition and update to the textbook that we denote here by "(AP)": L. C. Andrews and R. L. Phillips, *Laser Beam Propagation through Random Media*, 2nd edition, SPIE Press (2005). It presents many new and more-advanced topics that have emerged during the years since (AP) was published. The new material is largely based on the current authors' work with researchers from various universities, industrial companies, and government agencies over the last several years. Much of the new material has been published in peer-reviewed journals, but not all of it. And although the emphasis in this book is on atmospheric turbulence, as it is in (AP), the models contained within generally carry over to other random media like the ocean, where only the power spectrum needs to change. Our goal is that this new edition will serve as an organized reference in addition to (AP) for the optics community.

To a great extent, the material in the first two chapters is a brief summary of the fundamental concepts found in (AP). A certain amount of repetition from (AP) likewise appears in subsequent chapters in order to provide a smoother flow of the new material. However, some material in Chapter 1 is new, such as the introduction of *visibility* in connection with absorption and scattering of an optical wave and the HAP $C_n^2(h)$ profile model for slant-path propagation. Also, after a review of the Rytov theory and extended Rytov theory, Chapter 2 ends with some interesting results not contained in (AP) for the scintillation index of a *flattened Gaussian beam*.

Much of the new material in Chapters 3–6 is a consequence of taking *beam wander* into consideration. This includes refinement of the beam-wander models that were presented in (AP) and many new comparisons to computer simulation results. Beam wander is a topic that has been discussed in the literature since the 1960s and is still a topic of interest today. Of special significance is the *beam-wander-induced scintillation index* for both collimated and convergent beams. New models of wander-induced scintillation are compared here with computer simulation data acquired from several researchers. Beam-wander effects along horizontal paths with a constant refractive-index structure parameter are presented in Chapters 3–5 and along uplink paths to space in Chapter 6.

We introduce optical structures like lenses and aperture stops in Chapter 4 through the *ABCD ray matrix* approach. The matrix elements themselves become embedded with the *nondimensional Gaussian beam parameters* for the purpose of simplifying the algebra. Consequently, they don't explicitly appear in the derived statistical models after propagating through atmospheric turbulence. New models here include beam spot size, power in the bucket, power in the fiber, and beam-wander-induced scintillation, all in the *detector/image plane*.

In Chapter 5 we examine *probability density function* (PDF) *models* for the irradiance after passing through a finite aperture and, in some cases, including beam wander. Most early treatments of developing an irradiance PDF model were based on the infinite plane wave and spherical wave models and on the notion of a "point aperture." However, developing a PDF model for applications like optical communications and laser radar usually involves a Gaussian-beam wave and knowledge of the PDF after passing through a finite collecting lens at the receiver, producing a decrease in the irradiance fluctuations, known as *aperture averaging*. In this chapter we examine experimental and computer simulation data collected by several groups of researchers over a number of years at various ranges with differently sized receiver apertures and compare the results with many of the commonly cited PDF models under conditions of weak-to-strong irradiance fluctuations. In Chapter 6 we introduce additional PDF models for uplink propagation to space, distinguishing between *tracked* and *untracked* beams.

We update the theory for double-pass propagation of a beam through turbulence in Chapters 7 and 8, including reflection from *semi-rough targets* as well as *smooth targets*. Theoretical models more complete than those in (AP) are developed here under both weak and moderate-to-strong irradiance fluctuations for the enhanced backscatter (EBS) associated with a monostatic channel.

For beams close to the ground, it has been conjectured for years that optical turbulence is homogeneous (i.e., statistically stationary) and nearly isotropic, at least in the small scales. In fact, most of the mathematical models appearing in this text and in (AP) are based on that concept. At the same time, it has also been known that large, irregular turbulence inhomogeneities in the upper atmosphere appear to exhibit conditions for anisotropy. More recently, some researchers have found evidence that non-Kolmogorov and anisotropic conditions may also occur along horizontal propagation paths near the ground. In Chapter 9 we discuss these important topics of *non-Kolmogorov* and/or *anisotropic turbulence* near ground level. This is clearly an ongoing subject of interest that requires a lot more research to fully understand. Our approach here is simply to discuss some of the models recently developed for this type of turbulence, based in part on some experimental and computer simulation data, rather than attempt to present a more-detailed treatment involving models that have not been validated by experimental or computer simulation evidence.

In the last chapter, we discuss several of the commonly used instruments for measuring atmospheric parameters like the refractive-index structure parameter, inner scale, temperature, wind speed, heat flux, and so forth. The underlying mathematical theory for these measurement instruments is based on conventional isotropic Kolmogorov turbulence and includes both irradiance-based and phase-based techniques. The discussion is divided into methods based on direct measurement of turbulence and methods based on the optical effect of turbulence on a propagating beam. The discussion on scintillometers includes a novel three-aperture instrument for measuring the refractive-index structure constant, inner scale, and outer scale over long propagation paths, including slant paths from aircraft to ground. The chapter ends with a short discussion of path profiling.

The two appendices at the end of the text provide an easy reference to the major mathematical models developed in Chapters 2, 3, 4, and 9.

By far, the most fruitful method of analysis involving optical wave propagation through the atmosphere has been the *Rytov approximation*. Much of the material presented in this book is still based on the Rytov approximation because of the relatively simple formulation of statistical results that arise from it. However, it is a perturbation method that is generally limited to regimes of weak irradiance fluctuations. Numerous other approaches to optical wave propagation have been attempted by many researchers over the years with limited success, particularly with regard to developing analytical models for the scintillation index under moderate-to-strong irradiance fluctuations. In the late 1990s, the *extended Rytov theory* was first introduced for modeling the scintillation index under general conditions of irradiance fluctuations. The development of this technique, which builds off the Rytov approximation for scintillation—hence its name—was based on recognizing that proper filtering of the atmospheric spectrum into large-scale and small-scale contributions can lead to simple and useful results for the scintillation index. We use the extended Rytov method here for developing some of the new mathematical models for beam-wander-induced scintillation and scintillation index models after aperture averaging, and for EBS in double-passage propagation.

Acknowledgment

The authors wish to acknowledge Frida Strömqvist Vetelino and David Wayne, who provided outdoor experimental data for some of the graphs. Our thanks as well go to Szymon Gladysz for useful discussions on some material. Finally, we are also deeply indebted to the following individuals who provided the computer simulation data:

- Jaume L. Recolons and Frederico Dios, Universitat Politècnia de Catalunya, Barcelona, Spain

- Gary J. Baker, Lockheed Martin Advanced Technology Center, Palo Alto, California
- Ronald R. Parenti, Massachusetts Institute of Technology Lincoln Laboratories, Lexington, Massachusetts
- Szymon Gladysz, Fraunhofer IOSB, Ettlington, Germany
- Donald J. Link, MZA Associates, Albuquerque, New Mexico
- Daniel A. Paulson, University of Maryland, College Park, Maryland

Larry C. Andrews
Melissa K. Beason
May 2023

Chapter 1
Atmospheric Structure of Turbulence

1.0 Introduction

After the first demonstration of the laser in 1960, it was suggested that lasers be used to extend radio-frequency (RF) communication and radar techniques to the optical-frequency band. Initial areas of interest for laser applications included weaponry, ranging, remote sensing, target designation, imaging, and medical uses, among others. However, all systems that utilize optical waves, including ultraviolet (UV), visible, and infrared (IR), must take into account general propagation effects associated with the medium in which they propagate in addition to effects like diffraction associated with the wave itself. The propagation medium in many cases is the turbulent atmosphere for which index-of-refraction fluctuations along the propagation path cause a variety of deleterious changes on the wave.

Early investigations concerning the propagation of electromagnetic radiation and other waves through random media involved the propagation of starlight through the atmosphere and propagation of sound waves through the atmosphere and ocean. In addition, these investigations also involved propagation of microwaves through planetary atmospheres and propagation of radio waves through the ionosphere and interplanetary space. Thus, some of the theoretical work concerning the propagation of an optical wave in a turbulent or random medium was done prior to the introduction of the laser. By *random medium*, we mean one whose basic properties are random functions of space and time.

Astronomers (including Sir Isaac Newton) were among the first scientists to show interest in certain atmospheric effects, like the quivering of the image of an astronomical object at the focus of a telescope and temporal fluctuations in received irradiance (intensity), the latter commonly called *scintillation*. During the 1950s, Russian scientists began theoretical studies of scintillation to aid astronomers. These early theoretical studies

represents distance in kilometers. Extinction is defined as the reduction or attenuation in the intensity of radiation passing through the atmosphere.

A term related to the extinction coefficient is *visibility* V. This corresponds to the range in kilometers at which radiation at 550 nm is attenuated to 0.02 times the transmitted level. For a given wavelength λ [nm], the extinction coefficient is inversely related to visibility V through the empirical formula:[10]

$$\alpha(\lambda) = \frac{3.912}{V}\left(\frac{550}{\lambda}\right)^{q}; \quad q = \begin{cases} 1.6, & V > 50 \text{ km} \\ 1.3, & 6 \text{ km} < V < 50 \text{ km} \\ 0.585V^{1/3}, & V < 6 \text{ km}. \end{cases} \tag{1.8}$$

1.2 C_n^2 Profile Models as a Function of Altitude

Calculations of optical turbulence effects on an optical wave propagating through the atmosphere are necessary for modeling purposes and also for understanding the results of experimental data involving an optical wave. Because theoretical calculations rely heavily on optical turbulence models, it is important to have a good understanding of the basic behavior of the refractive-index structure parameter for the geographic area and altitude of interest. In applications involving propagation across a homogeneous terrain along a horizontal path, it is common to assume that the structure function parameter C_n^2 remains essentially constant along the path. This constant value can be reasonably estimated by using a *scintillometer* instrument that characterizes an average value of C_n^2 along the same path or a nearby parallel path (e.g., see Fig. 1.1 and Chapter 10). If propagation is along a vertical or slant path, or one that varies with height above the terrain, it is necessary to use certain analytical or numerical models of optical turbulence to describe changes in C_n^2 as a function of altitude h. These are known as $C_n^2(h)$ *profile models* and typically represent an average value of C_n^2 at a given altitude, based on various measurements made over the years.

In the daytime, optical turbulence is strongest near the ground, characterized in most geographic locations by C_n^2 on the order of 10^{-14} to $10^{-12}\,\mathrm{m}^{-2/3}$. During this period, the air temperature gradient is negative and, with increasing altitude, it has been observed that C_n^2 often decreases from the surface layer with an altitude dependence like $h^{-4/3}$. It is interesting that up to altitudes of a few hundred meters, the vertical profiles of C_n^2 above a desert or above a mountain are essentially the same, particularly if the mountain top is more of a plateau than a peak.[11] That is, in the daytime the mountain is simply an elevated surface. The C_n^2 profile model suggested by Walters and Kunkel[11] for the daytime convective boundary layer takes the form

Chapter 2
A Review of Gaussian-Beam Wave Propagation

2.0 Introduction

Optical wave propagation through the atmosphere is a subset of the more general study of electromagnetic wave propagation through random media. Random fluctuations in the index of refraction lead to spreading of the beam beyond that due to pure diffraction, beam wander, loss of spatial coherence, and random fluctuations in the irradiance and phase. Turbulent scale sizes on the order of the beam size and larger are responsible for beam wander and phase fluctuations, whereas scale sizes on the order of the first Fresnel zone or spatial coherence radius are the primary cause of irradiance fluctuations. Knowledge of the behavior of an optical wave in atmospheric turbulence is important in a variety of applications like imaging, free-space optical communications (FSOC), adaptive optics, remote sensing, and laser radar.

Many of the early theoretical treatments of optical wave propagation concentrated on simple field models such as an *unbounded plane wave* and *spherical wave*, the latter often taken as a "point source." However, in many applications, the plane wave and spherical wave approximations are not sufficient to characterize propagation properties of the wave, particularly when focusing and finite beam characteristics are important. In such cases, the *lowest-order Gaussian-beam wave* model is more characteristic of a laser beam, limiting forms of which lead to the plane wave and spherical wave models.

Much of the treatment in this chapter is a review of fundamental material such as that found in Ref. 1. In particular, we first review the basic transmitter (Tx) and receiver (Rx) *nondimensional beam parameters* used for describing propagation properties of a Gaussian-beam wave in free space (i.e., vacuum). Next, we introduce highlights of the *Rytov theory* as a means of characterizing beam propagation through atmospheric turbulence under weak irradiance fluctuations. Later in the chapter we present a summary of the *extended Rytov theory* developed primarily for extending the scintillation index under weak irradiance fluctuations into moderate-to-strong fluctuation regimes.

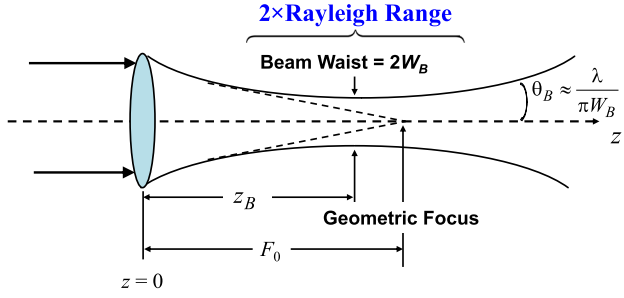

Figure 2.2 Convergent beam showing the beam waist, geometric focus, far-field divergence angle, and Rayleigh range (also called the confocal parameter) (adapted from Ref. 1).

In Section 2.3.1 we will once again examine the location of the beam waist, focus, and Rayleigh range but for a beam under the influence of atmospheric turbulence.

2.2 Rytov Theory

Gaussian-beam wave propagation through atmospheric turbulence has been studied at length through various theories that are normally restricted to certain regimes depending on the strength of the irradiance fluctuations. These fluctuations are classified as *weak irradiance fluctuations* or *strong irradiance fluctuations*, the latter sometimes being called *deep turbulence*. To distinguish between these regimes, we often use the *Rytov variance*, defined by

$$\sigma_R^2 = 1.23 C_n^2 k^{7/6} L^{11/6}, \tag{2.20}$$

where C_n^2 is the structure function parameter of refractive-index fluctuations. When $\sigma_R^2 < 1$, the optical wave is said to experience weak irradiance fluctuations and experiences moderate-to-strong irradiance fluctuations otherwise. If a Gaussian beam is focused, there are additional criteria that must be satisfied to classify the channel as weak irradiance fluctuations (see p. 140 of Ref. 1).

Of all the methods developed for optical wave propagation in atmospheric turbulence, the *Rytov approximation* has been the most fruitful. An early attempt using the Born approximation proved to be far more restrictive as to propagation path length and was soon abandoned. Other methods like geometrical optics were also less effective except for describing phase fluctuations. In this section we introduce the Rytov approximation[2] and restrict the analysis to beams in the pupil plane of a Rx system or beams that are incident on a target. It is generally assumed that atmospheric turbulence exists continuously along the line-of-sight path between the exit aperture of the Tx and the Rx at distance L, but this is not required.

A flow diagram of the primary statistical quantities related to the second-order and fourth-order field moments is presented in Table 2.1. Under weak

2.4 Scintillation Index

Irradiance fluctuations known as scintillation can be deduced from knowledge of the general *fourth-order field moment* of an optical wave (see Table 2.1). In the context of weak fluctuation theory, however, many early investigations into the scintillation characteristics of an optical wave were concerned with the log-amplitude variance σ_χ^2, or log-irradiance variance $\sigma_{\ln I}^2 = 4\sigma_\chi^2$. The majority of these early studies also primarily concerned the infinite plane wave and spherical wave models. Governing integrals for the Gaussian-beam wave scintillation index under weak irradiance fluctuations were developed in the mid-1960s, and some analytical solutions were published based on the Kolmogorov spectrum.[20–22] However, tractable analytical formulations for the scintillation index of a Gaussian-beam wave under general atmospheric conditions, including inner- and outer-scale effects, were not developed until much later.[11,23]

The *scintillation index* is the normalized variance of irradiance, defined in general by

$$\sigma_I^2(\mathbf{r}, L) = \frac{\langle I^2(\mathbf{r}, L)\rangle - \langle I(\mathbf{r},L)\rangle^2}{\langle I(\mathbf{r},L)\rangle^2} = \frac{\langle I^2(\mathbf{r}, L)\rangle}{\langle I(\mathbf{r},L)\rangle^2} - 1. \tag{2.73}$$

Under weak irradiance fluctuations, the scintillation index approximately equals the variance of log-irradiance and four times the log-amplitude variance. Knowledge of the scintillation index is important in that it is used in predicting detection probability, signal fade statistics, and bit error rate (BER) in FSOC systems and laser radar systems.

Because in this chapter we assume isotropy of the turbulence, the scintillation index will be circularly symmetric around the optical axis so that $\sigma_I^2(\mathbf{r}, L) \equiv \sigma_I^2(r, L)$. The scintillation index with anisotropy of turbulence is discussed in Chapter 9.

In Fig. 2.5(a) we present a photograph of a typical cross-section of the beam irradiance within the aperture diameter of a telescope after the beam has propagated 1000 m along a horizontal path 1–2 m above the ground. Here the coherent patches of the beam are easily recognized as contrasted with the dark areas, which represent deep fades of the irradiance. In Fig. 2.5(b) we show computer simulation results for a single-frame realization of the optical wave at several ranges between 1 km and 20 km, illustrating beam breakup at the longer ranges.

Unlike some of the quantities discussed in this chapter, the structure of the equations that describe irradiance fluctuations is highly dependent on the strength of the turbulence. Equations for the scintillation index derived from the Rytov process are only valid under weak irradiance fluctuations. In moderate-to-strong fluctuations another method must be used. We begin this section by presenting equations relevant to weak fluctuations, using the

Assuming isotropy of the turbulence, the moments can be simplified to

$$E_2(\mathbf{r}, \mathbf{r}) = 4\pi^2 k^2 \int_0^L \int_0^\infty \kappa \Phi_n(\kappa, z) \exp\left[-\frac{i\kappa^2}{2k}(\gamma - \gamma*)(L - z)\right] \times J_0(\kappa r|\gamma - \gamma*|) d\kappa dz \tag{2.123}$$

and

$$E_3(\mathbf{r}, \mathbf{r}) = -4\pi^2 k^2 \int_0^L \int_0^\infty \kappa \Phi_n(\kappa, z) \exp\left[-\frac{i\gamma\kappa^2}{k}(L - z)\right] d\kappa dz, \tag{2.124}$$

where $r = |\mathbf{r}|$. Using these equations for a plane wave ($\gamma = 1$), we find the phase variance to be given by

$$\sigma_S^2(L) = 2\pi^2 k^2 \int_0^L \int_0^\infty \kappa \Phi_n(\kappa, z) \left[1 + \cos\left(\frac{\kappa^2 z}{k}\right)\right] d\kappa dz. \tag{2.125}$$

With the geometrical optics approximation, we have $\cos(\kappa^2 z/k) \approx 1$. To evaluate the integral in Eq. (2.125) requires use of a power spectrum that has an outer-scale cutoff, or else the integral becomes unbounded. Using the von Kármán model [obtained from Eq. (1.4) with $\kappa_m \to \infty$],

$$\Phi_n(\kappa, z) = \frac{0.033 C_n^2(z)}{(\kappa^2 + \kappa_0^2)^{11/6}}, \qquad \kappa_0 \sim \frac{1}{L_0}, \tag{2.126}$$

we obtain the well-known result (see p. 83 of Ref. 31 or p. 635 of Ref. 1) relating the outer scale L_0 to the coherence diameter r_0, viz.,

$$\sigma_S^2 = 0.782 k^2 \kappa_0^{-5/3} \int_0^L C_n^2(z) dz \approx 1.85 \left(\frac{L_0}{r_0}\right)^{5/3}, \tag{2.127}$$

where we used $r_0 = [0.423 k^2 \int_0^L C_n^2(z) dz]^{-3/5}$ in deriving Eq. (2.127).

2.6 Flattened Gaussian Beams

Although our concentration thus far has been confined to the lowest-order TEM_{00} Gaussian-beam wave and the limiting forms of an infinite plane wave and spherical wave, many other beam shapes have received attention over the years from numerous researchers.[31–48] These other beam shapes include, but are not limited to, Hermite–Gaussian beams, Laguerre–Gaussian beams, annular beams, flattened Gaussian beams, Bessel beams, and so forth. This interest in other beam shapes is motivated in part by the search for methods and beam shapes that will improve system performance, particularly for FSOC and laser radar applications. Also, there are some applications, such as

Chapter 3
Beam Wander Along Horizontal Paths

3.0 Introduction

Over the years, various models have been developed for the scintillation index associated with a lowest-order Gaussian-beam wave.[1–9] However, although a lot of progress has been made in developing these models, there are still some beam-wave propagation issues that are not well understood. For example, weak-fluctuation Rytov theory predicts that the longitudinal component (or on-axis scintillation index) of a beam focused on a receiver (Rx) along a horizontal path continually decreases as the size of the laser-transmitter (Tx) aperture increases. At the same time, off-axis scintillation increases considerably. Similar theory also arises with the on-axis scintillation index behavior of certain collimated beams on an uplink path to a satellite,[4,5] and even along a horizontal path. Because this type of predicted behavior for a focused or collimated Gaussian beam seems physically unrealistic and generally has not been observed in experimental data, we reach the conclusion that conventional Rytov theory is incomplete with regard to these situations. Such theoretical uncertainties about the scintillation index bring us to the primary topic of this chapter—*beam wander*.

Beam wander associated with a propagating finite beam in the atmosphere has consequences for several characteristics of the beam irradiance in the plane of a Rx, including the *short-term* and *long-term spot size*, and the *scintillation index*. Beam wander was first investigated by researchers in the 1960s and has continued to the present.[10–24] This research led to reasonable models for centroid wander, but it was generally difficult early on to validate the impact of beam wander on the scintillation index because of the lack of sufficient and conclusive experimental data. Computer power has substantially increased in recent years such that it is now possible to study beam-wave propagation through simulation results that are generated from sophisticated wave-optics computer codes. Several published studies using computer simulations have been directed primarily at calculating the increase in scintillation that arises as a consequence of beam wander for both horizontal paths and uplink beams to space.[14–18,25]

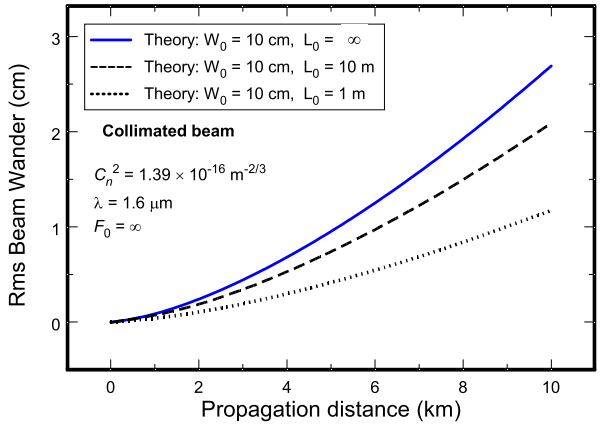

Figure 3.7 The rms total beam wander associated with a 10-cm collimated beam over a horizontal path of length 10 km with $C_n^2 = 1.39 \times 10^{-16}\,\mathrm{m}^{-2/3}$ and $\kappa_0 = 2\pi/L_0$. Outer-scale values of 10 m and 1 m are featured along with an infinite outer scale.

Even with a 10-m outer scale, the rms beam wander can be significantly reduced over long paths. Of course, a different choice of scaling constant in κ_0 can appreciably change the results from those illustrated in Fig. 3.7. For example, a scaling constant $\kappa_0 = 8\pi/L_0$, such as that used in the extended Rytov method,[6] would lead to a larger reduction in beam wander for the same outer scale L_0.

3.2 Mean Irradiance Profile and Beam Radius

The *mean irradiance profile* of a Gaussian beam with maximum amplitude A_0 at the Tx, derived through exact Rytov theory from the MCF under weak irradiance fluctuations, leads to

$$\langle I(r,\,L)\rangle = \underbrace{\frac{A_0^2 W_0^2}{W^2}\exp\left(-\frac{2r^2}{W^2}\right)}_{\text{Free space}}\underbrace{\exp\left[-1.33\sigma_R^2\Lambda^{5/6}{}_1F_1\left(-\frac{5}{6};\,1;\,\frac{2r^2}{W^2}\right)\right]}_{\text{Atmospheric effects}}, \tag{3.16}$$

where ${}_1F_1$ is a confluent hypergeometric function. However, this expression can usually be approximated by the Gaussian function,

$$\langle I(r,\,L)\rangle \approx \frac{A_0^2 W_0^2}{W_{LT}^2}\exp\left(-\frac{2r^2}{W_{LT}^2}\right), \tag{3.17}$$

where $W_{LT} = W(1 + 1.33\sigma_R^2\Lambda^{5/6})^{3/5}$ is the far-field *long-term spot radius* under weak-to-strong irradiance fluctuations (see Section 2.3). We expect the Gaussian approximation [Eq. (3.17)] to be a reasonable estimate of the mean

3.3 Wander-Induced Scintillation

Although *beam-wander-induced scintillation* was first studied in the late 1960s and 1970s, renewed interest in studying this phenomenon along various horizontal paths and uplink paths to space led to several new publications in later years. Estimates of the induced scintillation index from beam wander are given in Baker and Benson[15] and Baker,[16] but similar studies by Andrews et al.,[25] Recolons et al.,[18] and Andrews and Phillips[17] led to different analytical expressions for beam-wander-induced scintillation. In this chapter we only discuss the horizontal path case but consider both collimated and convergent beams along with computer simulation data. Uplink analysis will be taken up in Chapter 6.

3.3.1 Failure of the Rytov theory

Early on, it was common for researchers to assume through reciprocity arguments that conventional Rytov theory leading to angle-of-arrival fluctuations should also apply to beam wander.[11,21] Although beam wander is included in our expression for the long-term beam radius, the Rytov theory does not explicitly separate the small-scale contribution to spot size from the large-scale contribution that leads to beam wander. Understanding how beam wander contributes to the scintillation index is even less clear based on Rytov theory alone. Basically, the Rytov theory is incomplete in regard to beam wander and beam-wander-induced scintillation. Failure of the Rytov theory was previously discussed in Refs. 16, 26, and 27 in terms of what those authors called the D_1 region.

It was pointed out by Recolons et al.[18] that the region along the propagation path where Rytov theory falls apart for a convergent beam under weak irradiance fluctuations can be roughly approximated by the *longitudinal phase shift*, $\varphi = \tan^{-1}(\Lambda_0/\Theta_0)$, i.e.,

$$\text{Rytov theory excluded region: } \frac{\pi}{4} < \varphi < \frac{3\pi}{4}. \tag{3.22}$$

Although not exact, the longitudinal phase shift [Eq. (3.22)] based on free-space beam parameters provides a quick estimate of the region of concern for Rytov theory. Actually, this region [Eq. (3.22)] is similar to or almost the same as the Rayleigh range defined by Eq. (2.19). For example, the region defined by Eq. (3.22) and the Rayleigh range both correspond to the portion of the propagation path between 4.7 km and 5.3 km from the Tx for the beam illustrated in Fig. 3.8. The region described by Eq. (3.22) can also be interpreted as that region where the scintillation index associated with tracked and untracked beams separate (e.g., see Fig. 3.17 in Section 3.3.3).

In the remainder of Section 3.3, we consider the necessary correction to Rytov theory to account for the additional scintillation index resulting from beam wander for both tracked and untracked beams.

3.4 Flattened Gaussian Beams

Over the years, there have been a number of studies directed at the propagation of various beam profiles other than that of the lowest-order Gaussian beam.[28–35] Some studies have concentrated only on free-space propagation, but others have involved propagation paths through optical turbulence. The motivation for these various studies is not always the same. In the presence of atmospheric turbulence, for example, some of the studies were motivated by the question of whether a specifically shaped beam intensity profile might be more desirable in the applications relevant to optical systems.

In Section 2.6 we introduced the notion of a *flattened Gaussian beam* (FGB) as an approximation to a top-hat beam. At the Tx, the optical field of the FGB beam is defined by

$$U_{N0}(r, 0) = A_0 \exp\left(-\frac{r^2}{W_{N0}^2}\right) \sum_{n=0}^{N} \frac{1}{n!} \left(\frac{r^2}{W_{N0}^2}\right)^n, \tag{3.37}$$

where $W_{N0}^2 = W_0^2/(N+1)$, $N = 0, 1, 2, 3, \ldots$. This particular representation of the FGB reduces to a collimated TEM_{00} Gaussian beam when $N = 0$. Following the Gori model[29] as modified by Bagini et al.,[30] Cowan and Andrews[35] developed analytical expressions for the on-axis scintillation index of a perfectly tracked FGB and made comparisons with that of a standard TEM_{00} Gaussian-beam wave (see Section 2.6.2). Here we further examine the FGB in regard to a perfectly tracked beam and also consider the results of beam-wander-induced scintillation on an untracked beam. Computer simulation data are compared with the theoretical FGB model under perfect tracking, and computer simulation data for an untracked FGB are compared with the theoretical model for a TEM_{00} Gaussian beam. No scintillation theory currently exists for the untracked FGB.

3.4.1 Beam wander

Cowan and Andrews[35] discuss the spot size associated with a FGB and find that the initial spot size at the Tx defined by W_0 for a TEM_{00} Gaussian beam is nearly the same as that for a FGB. In particular, given FGBs of order 5 and 10, the calculated spot sizes were $0.936W_0$ and $0.943W_0$, respectively, just slightly smaller than W_0. Because of this, it was concluded that there would be little difference in beam wander associated with a FGB as compared with that presented in Section 3.1 for a standard Gaussian beam. Even changing the value of N makes little difference. To illustrate these facts, we show computer simulation results[34] of centroid beam wander in Fig. 3.20 for a 3-cm FGB compared with that described by Eq. (3.8) for a conventional collimated Gaussian beam. The wavelength is $1.06\,\mu\mathrm{m}$, $C_n^2 = 1 \times 10^{-14}\,\mathrm{m}^{-2/3}$, and

Chapter 4
ABCD Ray Matrices: Atmospheric Propagation

4.0 Introduction

In this chapter we introduce Gaussian-beam wave propagation through various optical structures such as lenses and aperture stops that are arbitrarily distributed along the propagation path but perfectly aligned with the optical axis. If we characterize the optical elements by 2×2 matrices, called *ABCD ray matrices*,[1–6] we can continue to use the *paraxial approximation* and *Huygens–Fresnel integral*. In free space this leads to a Gaussian-beam wave at the end of the path even though the beam passes through one or more of these optical elements. That is, the Gaussian nature of the beam model is preserved with the use of these matrices, unlike what actually occurs with *hard-aperture* structures. Fortunately, the *ABCD* ray matrix method also permits us to include the presence of optical turbulence along the path—over only a portion of the path or everywhere between input and output planes. The use of these matrices leads to generalizations of the spectral representations that arise in the Rytov approximation.

4.1 *ABCD* Ray Matrices

An effective way to discuss Gaussian-beam wave propagation through various optical elements like lenses and aperture stops is by the use of *ABCD ray matrices*. The use of such matrices allows us to describe the propagation of a Gaussian beam through a train of optical elements by utilizing the *cascade scheme* of multiplying successive matrix representations of each optical element. In particular, if there exists a sequence of N such elements distributed along the propagation path, including those that represent free-space line-of-sight sections between optical elements, the entire propagation path can be represented by a single *ABCD* ray matrix of the form

$$E_3(\mathbf{r}_1, \mathbf{r}_2) = -4\pi^2 k^2 L_1 \int_0^1 \int_0^\infty \kappa \Phi_n(\kappa) J_0(\gamma_1 \kappa \rho) \exp\left[-\frac{i\kappa^2}{k}\gamma_1 B_1(\xi)\right] d\kappa d\xi$$
$$- 4\pi^2 k^2 L_2 \int_0^1 \int_0^\infty \kappa \Phi_n(\kappa) J_0(\gamma_2 \kappa \rho) \exp\left[-\frac{i\kappa^2}{k}\gamma_2 B_2(\xi)\right] d\kappa d\xi, \tag{4.33}$$

where $\rho = |\mathbf{r}_1 - \mathbf{r}_2|$ and $J_0(x)$ is a Bessel function of the first kind. Because the integral for $E_1(0, 0)$ is proportional to the phase variance under a geometrical optics approximation (no diffraction effects), it is independent of beam characteristics and any optical elements distributed along the path—hence, it takes the straightforward form given by Eq. (4.31).

If we are interested only in a system (Fig. 4.1) where the distance between the Gaussian lens and detector plane at the Rx is short enough that atmospheric effects can be ignored, it is not necessary to include the integrals in Eqs. (4.31) through (4.33) with the subscript "2" for this application. On the other hand, if the lens is closer to the Tx such that atmospheric effects are significant only after the lens, then the integrals in Eqs. (4.31) through (4.33) with subscript "1" can be ignored. Finally, when atmospheric turbulence must be accounted for in front of and behind the lens, both sets of integrals in Eqs. (4.31) through (4.33) will be necessary.

4.3 Detector/Image Plane Analysis

Figure 4.2 is basically a simplified diagram of a free-space optical communication (FSOC) system. By treating the lens as part of the Rx system, atmospheric effects are taken into account only in front of the lens—hence, we need only the parameters γ_1 and $B_1(\xi)$ along the propagation path, defined by Eqs. (4.26) and (4.28), respectively. Accordingly, we now focus our

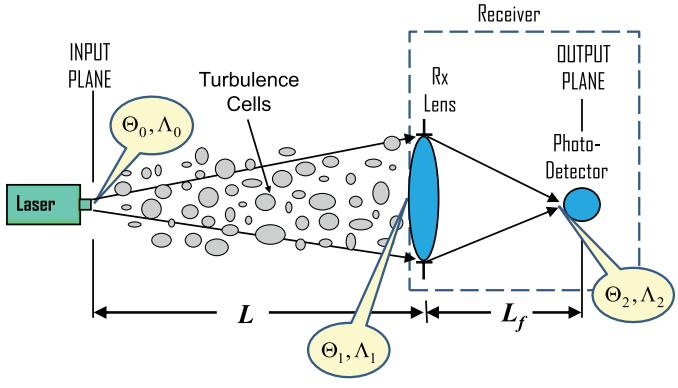

Figure 4.2 Propagation path through a Rx Gaussian lens (adapted from Ref. 2).

Beam-wander-induced scintillation is not an issue in either case but may become an issue with certain Gaussian-beam waves, as is discussed in Section 4.4.4.

4.4 Extended Rytov Theory

The extended Rytov approximation was discussed in Section 2.4.2 as a method for extending results for the Rx-pupil-plane scintillation index into moderate-to-strong irradiance fluctuation regimes. Here we wish to further pursue this approach in the detector/image plane with regard to aperture averaging using the *ABCD* matrix method. The system under study is shown in Fig. 4.2.

4.4.1 Aperture averaging: no inner-/outer-scale effects

The decrease in scintillation associated with increasing the aperture of the telescope collecting lens had been recognized in early astronomical measurements.[10] For such systems, the infinite plane wave was an appropriate optical wave model for light coming from a distant star. Many early investigations into optical wave propagation along terrestrial paths also considered the infinite plane wave as a reasonable approximation for a large, near-field ($\Lambda_0 \ll 1$), collimated Gaussian-beam wave. Likewise, the spherical wave model for terrestrial paths was associated with a small divergent beam (point source) or far-field beam ($\Lambda_0 \gg 1$).

Our approach here follows that in Section 2.4.2 where the extended Rytov theory was introduced for the scintillation index. However, we first ignore the effects of inner/outer scales and assume that

$$\sigma_I^2(D_{Rx}) = \exp[\sigma_{\ln X}^2(D_{Rx}) + \sigma_{\ln Y}^2(D_{Rx})] - 1. \tag{4.50}$$

By use of the large-scale filter function [Eq. (2.97)], for the case of an infinite *plane wave*, we are led to the large-scale log-irradiance flux variance,[11]

$$\begin{aligned}\sigma_{\ln X}^2(D_{Rx}) &= 8\pi^2 k^2 L \int_0^1 \int_0^\infty \kappa \Phi_n(\kappa) \exp\left(-\frac{\kappa^2}{\kappa_X^2}\right) \exp\left(-\frac{D_{Rx}^2 \kappa^2}{16}\right) \\ &\quad \times \left[1 - \cos\left(\frac{L\kappa^2 \xi}{k}\right)\right] d\kappa d\xi \\ &\approx \frac{0.16\sigma_R^2 \eta_X^{7/6}}{\left(1 + d^2 \eta_X/4\right)^{7/6}}, \quad \kappa \ll \kappa_X,\end{aligned} \tag{4.51}$$

where

Chapter 5
Analysis of Probability Density Function Models

5.0 Introduction

The reliability of a free-space optical communications (FSOC) system in atmospheric turbulence can be deduced from a mathematical model of the *probability density function* (PDF) of the irradiance (also called intensity). Scintillation can lead to power losses at the pupil plane of a receiver (Rx) and eventually to fading of the received signal below a specified threshold in the detector plane. Consequently, one of the goals in studying optical wave propagation through the atmosphere is the identification of a tractable PDF model for the irradiance under all irradiance fluctuation conditions. Over the years, an abundance of PDF models has been proposed with varying degrees of success. Of particular importance are (1) the accuracy of the PDF model in the low-intensity portion of the tail that leads to the probability of fade and (2) the bit error rate in the design of FSOC systems. Accuracy in the high-intensity portion of the tail is also important for eye-safety calculations and to recognize the potential for equipment damage through random surges.

One of the earliest PDF models that gained wide attention was the lognormal (LN) distribution,[1] but this model is generally restricted to regimes of weak irradiance fluctuations. However, Wheelon[2] has called into question the fit of the LN model even under weak irradiance fluctuations because including second-order and first-order perturbations in the Rytov approximation can cause a mismatch in the tails of the PDF. Other models that included both weak and/or strong irradiance fluctuations were the *K*-distribution,[3] the lognormal-Rician distribution (also called Beckman's PDF),[4] the gamma-gamma (GG) distribution,[5] and the inverse Gaussian gamma (IGG) distribution,[6] among a host of other models.[7] Both the lognormal-Rician and the GG distributions have provided good fits to computer simulation data for small Rx apertures with incident plane and spherical wave models[5] (see also pp. 371–380 of Ref. 8).

Most PDF models have been proposed for the receiver pupil plane, not including passage to the detector plane with a finite Rx aperture. This is

5.3.3 Bit-error-rate data analysis

It is well known that the performance of a digital FSOC system can be evaluated in part by computing the *bit error rate* (BER). In addition to PDF analysis, the authors of Ref. 9 examined the mean BER at 75- and 100-km ranges for on–off keying (OOK) using the relation

$$\langle \mathrm{BE}R\rangle = \frac{1}{2}\int_0^\infty p_I(u)\mathrm{erfc}\left(\frac{\langle \mathrm{SN}R\rangle u}{2\sqrt{2}}\right)du, \tag{5.16}$$

where $\langle \mathrm{SNR}\rangle$ is the mean signal-to-noise ratio and $p_I(u)$ is the test PDF. The function erfc(x) is the complementary error function.[13] The authors provided plots as a function of mean SNR extended to slightly beyond 30 dB for the single-pixel aperture diameter and $3\rho_0/2$ with $C_n^2 = 1\times10^{-16}$ and $10^{-15}\,\mathrm{m}^{-2/3}$. Again, the GG distribution better matched the single-pixel data and the smaller C_n^2 value at 75 km, but was a worse fit to the larger C_n^2 value. In fact, the mean BER simulation data fell between the LN and GG models for the larger C_n^2 value. The LN model matched the data better at 100 km for the larger aperture and both C_n^2 values.

5.4 Experimental Data in a Maritime Environment: Tracked Collimated Beam

A long-range propagation investigation was performed by Nelson et al.[20] over ranges from 5.1 to 17.8 km. In this case the investigation was with measured experimental data in a maritime environment. This group of researchers compared data to LN, GG (with aperture averaging labeled as $\mathrm{GG_A}$), and a *gamma-Laguerre* (GL) *distribution*. The GL distribution is defined by

$$P_{GL}(I) = P_G(I)\sum_{n=0}^{\infty} U_n L_n^{(\beta-1)}\left(\frac{\beta I}{\mu}\right), \quad I>0, \tag{5.17}$$

where P_G(I) is the gamma distribution, U_n is a weighting coefficient, and $L_n^{(\beta-1)}(x)$ denotes a generalized Laguerre polynomial.[13] The parameter μ is the mean intensity and β is the reciprocal of the scintillation index. The detectors were classified as either a power-in-bucket (PIB) or a power-in-fiber (PIF) adaptive optics (AO) detector. In all cases the beam was tracked using AO.

5.4.1 Results

The propagation path was a shore-to-ship, bi-directional, optical link near Wallops Island, Virginia on the Atlantic Coast. A 1550-nm beam of diameter 10 cm was transmitted over various ranges as indicated below. Numerical results from the measured data were divided into two cases.

While the two smallest apertures had distributions that were right-tailed, the largest of the apertures was more symmetric. In the next section we will see that with beam wander, the trend of changing skewness further continues with larger apertures, actually becoming left-tailed for the largest apertures studied. Unfortunately, due to the size limitations of the camera array, it was not possible to study larger aperture sizes for the experimental data set presented above.

5.6 Numerical Comparison of PDF Models: Untracked Collimated Beam

Much of the early research to determine the best PDF model under weak or moderate-to-strong irradiance fluctuations concentrated on PDF models describing either a plane wave or a spherical wave incident on a point aperture.[5,21–24] However, realistic FSOC systems generally utilize a collimated beam to both maximize energy density at the Rx and increase security. Realistic systems also use large apertures to reduce signal dropout caused by scintillation. In this section we continue our analysis of various PDF models based on computer simulation data involving a collimated Gaussian beam over a 2-km path. The methodology used to generate the data is described in Beason et al.[25] Beam wander was *not* removed from the data in this analysis.

One of the fundamental observations of the work in Ref. 25 was the change in skewness of the irradiance-flux PDF, which occurs when large apertures are used with a Gaussian beam that also experiences beam wander. In particular, the authors found a consistent change in the sign of the skewness of the empirical distribution (generated from simulation data) at an aperture radius approximately equal to the FZ plus beam centroid wander under weak irradiance fluctuations, or the coherence radius plus beam centroid wander in moderate-to-strong irradiance fluctuations. Skewness indicates the asymmetry of the distribution. For instance, a normal distribution is symmetric and therefore has zero skewness, while a right-tailed distribution such as lognormal has a positive skewness.

5.6.1 Impact of PDF model on mean BER and fade probability

Performance metrics such as mean BER $\langle \text{BER} \rangle$ and probability of fade $\Pr_{fade}$ for FSOC applications using intensity modulation and direct-detection devices were theoretically calculated in Ref. 26 based on the PDF models in Section 5.1. Theoretical calculations based on the wrong PDF model can result in significant errors in the prediction of performance metrics. For example, most of the past work with these models did not consider the change in skewness of the distribution as the Rx aperture size increased. Consequently, positively skewed distributions (right-tailed) were likely used to model scenarios where the true statistics were negatively skewed (left-tailed).

Chapter 6
Beam Wander Along Uplink Paths

6.0 Introduction

In Chapter 3 we discussed beam-wander effects on a propagating Gaussian-beam wave along a horizontal path. In the current chapter we wish to continue that analysis for uplink paths to space or to an aircraft.

For many years there has been interest in the possibility of using high-data-rate optical transmitters for free-space optical communications (FSOC). Applications that can benefit from FSOC systems are those that have platforms with limited weight and space, require very high data links, and must operate in an environment where fiber-optic links are not practical, such as an uplink/downlink path to/from an aircraft or satellite. This interest in FSOC prompted a number of early investigations into laser communication systems for uplink and downlink channels that continue today.[1–20]

Despite the progress that has been made over the years in developing mathematical models for laser propagation, there are still some aspects of beam wave propagation that are not well understood, particularly in regard to uplink collimated beams. For example, the conventional weak-fluctuation Rytov theory predicts that the on-axis scintillation index of a mid-size collimated beam on an uplink path to a satellite should lead to greatly reduced values of the scintillation index.[1,2,8] Although this was questioned by early researchers, we now know through more recent computer simulation studies that this is not true in the presence of beam wander. For example, Dios et al.[13] show through a computer simulation study that the on-axis log-amplitude variance of a collimated beam from ground to space can be much greater than that predicted by the conventional Rytov theory when beam wander is present. Baker and Benson[14] also show similar discrepancies in the on-axis scintillation index between that predicted by the conventional Rytov theory and their numerical wave-optics simulation results in an uplink path to low Earth orbit (LEO). By adding wander tracking to their wave-optics simulation code, Baker and Benson found that the on-axis simulation results and Rytov

$$p_I(I) = \frac{1}{\Gamma(m)I}\left(\frac{mI}{\langle I(0,L)\rangle}\right)^m \exp\left(-\frac{mI}{\langle I(0,\,L)\rangle}\right), \quad I > 0, \tag{6.29}$$

where the parameter m is the reciprocal of the on-axis scintillation index (tracked or untracked); i.e.,

$$m = \frac{1}{\sigma_I^2(0,\,L)}. \tag{6.30}$$

6.4 PDF Models for Uplink Beams—II

In this section we restrict the PDF models mostly to beam sizes defined by $0.1 < 2W_0/r_{0\mathrm{T}} < 10$ in which beam-wander-induced scintillation is likely to occur. Early researchers developed some PDF models that accounted for the presence of beam wander, or beam jitter, at the Rx plane.[23–26] In particular, it was suggested that the instantaneous irradiance u at distance L from the Tx can be modeled by a Gaussian function: $u = \exp[-(x^2 + y^2)/2c\sigma^2]$. Here, x and y are Gaussian random displacements with zero means and equal jitter variance σ^2. The parameter c was originally related to the squared ratio of beam spot size to jitter. However, it is shown below that the parameter c can also be directly related to the on-axis scintillation index that occurs in the presence of beam wander.[19] Through a series of transformations of random variables, the PDF for u becomes the *modified beta distribution* (see Appendix at the end of chapter):

$$p_1(u) = cu^{c-1}, \quad 0 < u \le 1. \tag{6.31}$$

To derive an expression for c based on scintillation, we start by assuming that the irradiance $\hat{E}$ with beam-wander-induced scintillation can be expressed as a modulation of the normalized irradiance without beam wander. Thus, we write the irradiance as

$$\hat{E} = Zu, \tag{6.32}$$

where $Z = I/\langle I\rangle$ is the normalized irradiance without beam wander. Assuming statistical independence of Z and u, the first two moments of the irradiance [Eq. (6.32)] can be expressed in the form

$$\begin{aligned} \langle \hat{E}\rangle &= \langle Z\rangle\langle u\rangle = \frac{c}{1+c}, \\ \langle \hat{E}^2\rangle &= \langle Z^2\rangle\langle u^2\rangle = [1 + \exp(\sigma^2_{\ln X} + \sigma^2_{\ln Y})]\left(\frac{c}{2+c}\right), \end{aligned} \tag{6.33}$$

where $\sigma^2_{\ln X}$ and $\sigma^2_{\ln Y}$ are defined by Eq. (6.28) and $\langle Z\rangle = 1$. In obtaining Eq. (6.33), we have used Eq. (6.31) to calculate the first two moments:

$$\langle u\rangle = \frac{c}{1+c}, \qquad \langle u^2\rangle = \frac{c}{2+c}. \tag{6.34}$$

Chapter 7
Double-Pass Propagation: Smooth Targets

7.0 Introduction

Conventional *radar systems* came into being during the mid-1930s. Their primary application was the detection, ranging, and tracking of aircraft. Since that time radar has become a necessary tool in modern warfare, commercial aircraft traffic control, remote atmospheric sensing, law enforcement applications, unmanned aerial vehicles (UAVs) or drones, and self-driving cars, among others. With the introduction of the laser in 1960, the radar techniques were soon carried over to the optical portion of the electromagnetic spectrum. *Laser radars*, or *lidar systems*, constitute a direct extension of conventional radar techniques (microwave frequencies) to very short optical wavelengths (including ultraviolet, visible, near-IR, mid-IR, and far-IR). Not surprisingly, the theory for laser radar is based partly on the theory developed by Marcum and Swerling[1] for microwave radars.

A *monostatic system* is a system in which the transmitter (Tx) and receiver (Rx) are co-located, often referred to as a *transceiver*. In such a system the transmitted wave must traverse the same atmospheric path twice in opposite directions—once in the forward direction to the target and, upon reflection, back to the Rx in the opposite direction. When the Tx and Rx are separated in the plane of the Rx by much more than a Fresnel zone, this is called a *bistatic system*.

For double-pass propagation in a monostatic system, wave properties are largely determined by turbulence-induced cross-correlations between the incident and reflected waves that lead to a variety of optical consequences such as the *backscatter amplification effect* (BSAE) and an *increase* in the *irradiance fluctuations* of the reflected waveform. These two effects are also widely known as *enhanced backscatter* (EBS). Optical waves propagating twice in opposite directions through statistically dependent inhomogeneities of a random medium, leading to EBS, have been the subject of numerous theoretical and experimental studies since the early 1970s.[2–20]

Mathematical models developed for describing the statistical characteristics of the illumination beam on a target are presented in Chapter 2. These models are based on *conventional Kolmogorov turbulence*, including the

$$\sigma_{I,R}^2(0,\,L) = 8\pi^2 k^2 L \int_0^1 \int_0^\infty \kappa\Phi_n(\kappa)\exp\left(-\frac{\Lambda_2 L\kappa^2\xi^2}{k}\right) \times \left\{1-\cos\left[\frac{L\kappa^2}{k}\xi\left(1-\bar{\Theta}_2\xi\right)\right]\right\} d\kappa d\xi$$
$$= 3.86\sigma_R^2(L)\mathrm{Re}\left[j^{5/6}{}_2F_1\left(-\frac{5}{6},\,\frac{11}{6};\,\frac{17}{6};\,\bar{\Theta}_2+j\Lambda_2\right)-\frac{11}{16}\Lambda_2^{5/6}\right]. \tag{7.122}$$

The remaining cross-correlation terms in Eq. (7.120) evaluated on the optical axis are the same for a plane mirror and a retroreflector, both reducing to

$$C_I^{iR}(0,\,L) = 8\pi^2 k^2 L\mathrm{Re}\int_0^1\int_0^\infty \kappa\Phi_n(\kappa)\exp\left[-\frac{\Lambda_2 L\kappa^2(1+\xi^2)}{2k}\right] \times \left\{\exp\left[-\frac{jL\kappa^2}{2k}\left(1+\Theta_2-2\xi+\bar{\Theta}_2\xi^2\right)\right] - \exp\left[-\frac{jL\kappa^2}{2k}\left(1+\Theta_2-\bar{\Theta}_2\xi^2\right)\right]\right\} d\kappa d\xi$$
$$= 3.97\sigma_R^2(L)\mathrm{Re}\int_0^1\left\{\left[\Lambda_2(1+\xi^2)+j\left(1+\Theta_2-\bar{\Theta}_2\xi^2\right)\right]^{5/6} - \left[\Lambda_2(1+\xi^2)+j\left(1+\Theta_2-2\xi+\bar{\Theta}_2\xi^2\right)\right]^{5/6}\right\} d\xi, \tag{7.123}$$

where numerical integration is suggested to complete the last step.

In Fig. 7.12 the scaled on-axis scintillation index [Eq. (7.120)] of a reflected plane wave is plotted as a function of nondimensional target size at a range of 10 km. Note that the scaled scintillation index is 5.22 for very large targets and 2.05 for small (point) targets. Also shown for contrast is the scaled scintillation index for a reflected spherical wave (dashed line). In the spherical wave case, the scaled scintillation index for large targets is 2.88 and for small targets is 1.6. The reflected plane wave scintillation index for most targets is somewhat greater than that for a reflected spherical wave, especially for larger targets ($\Omega_T < 0.5$).

7.4 Unresolved (Point) Target

When the transverse dimension of the target is significantly smaller than the size of the first Fresnel zone (i.e., $\Omega_T \gg 1$), this is considered an *unresolved small target*, commonly called a *point target*. In this case, there is no distinction between a mirror and retroreflector. Also, the echo wave behaves similarly to a spherical wave, with the target acting as a pseudo-point source.

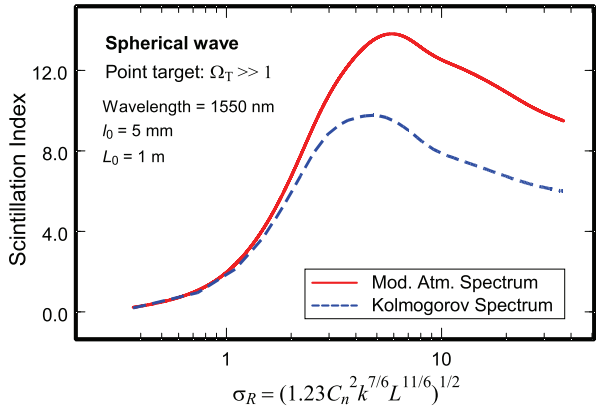

Figure 7.21 The monostatic channel on-axis scintillation index in the Rx plane plotted as a function of the square root of the Rytov variance. The target is a point target, and results are based on a Kolmogorov spectrum (dashed line) and the modified atmospheric spectrum (solid line) (adapted from Ref. 22).

peak scintillation index has reached double-digit values around 13, which is much higher than ever observed for a one-way propagation path. Even the Kolmogorov spectrum result without inner-/outer-scale values (dashed line) is larger than that of one-way propagation with the inclusion of inner-/outer-scale effects.

7.7 Detector Plane Analysis

In Section 7.1.3 we examined the free-space propagation properties associated with a Gaussian-beam wave in the detector plane, as illustrated in Fig. 7.1. This included the beam parameters Θ_3 and Λ_3 defined by Eq. (7.7). By assuming that the photo-detector is located in the image plane, we set $\Theta_3 = 0$ from which it follows that $\Lambda_3 = L/[L_f(\Lambda_2 + \Omega_{Rx})]$ and $1/L_f = 1/F_{Rx} + 1/F_2$. In this section we restrict the analysis to a retroreflector target or a point target, mostly under weak irradiance fluctuations.

7.7.1 Path amplitude parameters

The MCF associated with a reflected wave from an on-axis smooth target in the plane of the detector can once again be expressed in the form of Eq. (7.49). However, the path amplitude ratios γ_a^i, γ_a^R and γ_b^i, γ_b^R, which appear in Eqs. (7.32) and (7.45), respectively, must be redefined for the detector plane. The same is true for the matrix elements $B_a^i(\xi)$, $B_a^R(\xi)$ and $B_b^i(\xi)$, $B_b^R(\xi)$.

To begin, we first recall that the overall $ABCD$ matrix that characterizes the free-space beam in the detector plane is (see Section 7.1.1)

Chapter 8
Double-Pass Propagation: Semi-Rough and Diffuse Targets

8.0 Introduction

Incident light on a rough surface may be reflected specularly, diffusely, or both. The proportion of diffuse reflection to specular reflection depends on the relation between the roughness of the surface and the wavelength of the incident radiation. In Chapter 7 we considered laser beam reflection from only smooth targets like mirrors and retroreflectors. Reflection from such surfaces is called *specular*. However, in most laser radar systems the target is not smooth but has a certain surface roughness associated with it.[1–3] Therefore, in addition to atmospheric turbulence along the path to and from the target, the target itself can impose a certain phase distortion on the echo beam. That is, the roughness of a target plays an important role in determining the nature of the return echo beam. If the surface of a target is considered rough on the scale of an optical wavelength, this causes the reflected wave to be scattered back in all directions. Such a surface is called a *diffuse surface* or *Lambertian surface*. The echo beam will then contain many coherent components, each arising from a different microscopic element of the surface. Interference of the coherent components results in a granular pattern of irradiance at the Rx pupil plane known as *speckle*. The correlation area of the speckle in the pupil plane or image plane is important because it may be used to identify certain target characteristics and/or atmospheric components.

Surface roughness is often defined in terms of surface height deviations from some average value. Hence, it has been customary in modeling a rough surface to start with a particular height model of the surface like a Gaussian density function (see pp. 70–98 of Ref. 1). However, this may not be necessary in many cases. For example, to distinguish between surfaces with approximately the same height variation, it may be useful instead to define a characteristic lateral scale size called the *correlation radius* l_c. The correlation radius is typically

$$\rho_{DP,\text{speckle}} = \left(\frac{4\lambda L_f}{\pi D_{Rx}}\right)\sqrt{1+\Omega_{Rx}\Omega_T} = \left(\frac{1.27\lambda L_f}{D_{Rx}}\right)\sqrt{1+\Omega_{Rx}\Omega_T}. \quad (8.31)$$

8.2 Ladar Model in Optical Turbulence: Weak Irradiance Fluctuations

We now consider the semi-rough target in the presence of optical turbulence, which we assume is statistically independent of the fluctuations associated with the random rough target surface. Our analysis is limited to the Rx pupil plane.

8.2.1 Beam spot size and BSAE: spherical wave

We further restrict the analysis here to the case where the target is in the far field of the Tx. Hence, the illumination beam can be approximated by a *spherical wave*. Nonetheless, the backscatter amplification effect (BSAE) associated with a reflected spherical wave from a semi-rough target should have characteristics similar to those of a small reflected Gaussian-beam wave.

By using the phase screen model leading to Eq. (8.10), we obtain the MCF in the presence of atmospheric turbulence, given by

$$\Gamma_2(\mathbf{r}_1, \mathbf{r}_2, 2L) = \Gamma^0_{2,RP}(\mathbf{r}_1, \mathbf{r}_2, 2L)\Gamma_{2,\text{atm}}(\mathbf{r}_1, \mathbf{r}_2, 2L), \quad (8.32)$$

where $\Gamma^0_{2,RP}(\mathbf{r}_1, \mathbf{r}_2, 2L)$ is defined by Eq. (8.10) and $\Gamma_{2,\text{atm}}(\mathbf{r}_1, \mathbf{r}_2, 2L)$, assumed to be statistically independent of the semi-rough target surface, is the MCF of an incident spherical wave due to atmospheric effects. Based on Eq. (8.32), the *mean irradiance* of a reflected spherical wave is given by ($\mathbf{r}_1 = \mathbf{r}_2 = \mathbf{r}$)

$$\langle I(\mathbf{r}, 2L)\rangle_{\text{Monostatic}} \approx \frac{4\pi R_s^2 W_T^2}{k^2 W_{2,LT}^2\left[1+4q_c\left(\frac{\Omega_T}{4+\Omega_T^2}\right)\right]} \times \exp\left\{-\frac{2r^2}{W_{2,LT}^2\left[1+4q_c\left(\frac{\Omega_T}{4+\Omega_T^2}\right)\right]}\right\}\exp\left[B_I^{iR}(\mathbf{r}, L)\right]. \quad (8.33)$$

The term $W_{2,LT}$ is the far-field long-term spot size of a *smooth target* in the pupil plane of the Rx, defined by (see Section 7.2.3.2)

$$W_{2,LT} = W_T\sqrt{4+\Omega_T^2}\left[1+2.65\sigma_R^2(L)\left(\frac{\Omega_T}{4+\Omega_T^2}\right)^{5/6}\right]^{3/5}. \quad (8.34)$$

Also taking into account the semi-rough target, the *long-term spot size* in the Rx pupil plane becomes

Chapter 9
Non-Kolmogorov Turbulence

9.0 Introduction

The *atmospheric boundary layer* (ABL) is that region up to roughly 1–2 km above the Earth's surface where heating of the surface leads to convective instability. The *free atmosphere* refers to that portion of the atmosphere above the ABL in which the effect of the Earth's surface friction on the air motion is negligible. Although ignored thus far in our theoretical development, experimental measurements in the free atmosphere have shown evidence of non-Kolmogorov and anisotropic turbulence.[1–4] It is now known that in the upper atmosphere the irregularities of turbulence in the horizontal directions can be many times larger than those in the vertical direction (see pp. 80–84 of Ref. 5). We illustrate this idea by the schematic of large turbulent cells shown in Fig. 9.1 as a function of altitude. Near the Earth's surface, the large turbulent cells, or "eddies," are more symmetric but become more elongated with altitude.

For the ABL closer to the ground, it has been conjectured that optical turbulence is homogeneous and nearly isotropic.[6] Consequently, the Kolmogorov spectrum model near the ground is generally a good assumption within the inertial subrange. Nonetheless, this is not necessarily always the case in the close proximity of a hard boundary surface such as just above ground.[7] In fact, recent horizontal-path measurements near the ground have shown that non-Kolmogorov and anisotropic conditions can sometimes exist.[7–9]

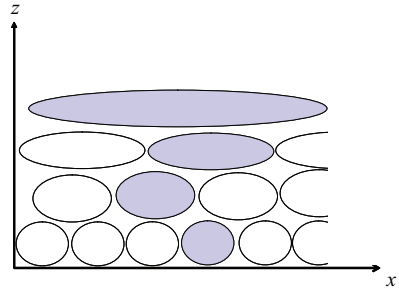

Figure 9.1 Schematic depicting the anisotropic nature of the upper atmosphere by showing the largest turbulent cells (eddies) as a function of altitude (adapted from Ref. 22).

In developing Eq. (9.53), we assumed that the high-spatial-frequency bump had minimal dependence on α. Both Eqs. (9.47) and (9.53) assume that the anisotropy is constant over all scale sizes.

The inner scale can have a significant impact on the relationship $\beta = \tilde{C}_n^2/C_n^2$ as discussed in Ref. 19. In this case, to force equal scintillation indices, we must consider the impact of the inner scale on scintillation by forcing the relationship $\sigma_I^2(l_0) = \tilde{\sigma}_I^2(\alpha, \mu_x, \mu_y, l_0)$.

Anisotropy as presented throughout the remaining sections of this chapter is based on the assumption that it is constant across all scale sizes in the spectral models. A spectral model with anisotropy decreasing with a decrease in scale size is probably more physically realistic, as discussed by Toselli.[33] However, the form of the transition of anisotropy is highly dependent on boundary conditions and currently is not well understood. For our treatment here, we have followed the current trend of the literature by considering a constant anisotropy ratio across all scales; however, we present the equations in a form that the reader can extend to new spectral models as they are discovered.

9.4 Beam Propagation in Anisotropic Non-Kolmogorov Turbulence

In this section we develop beam statistical quantities analogous to those in Section 9.2 based on the general anisotropic spectrum model [Eq. (9.44)] extended over the range $0 < \kappa < \infty$. By simply setting $\mu_x = \mu_y = 1$, our results reduce to those based on the isotropic spectrum model [Eq. (9.5)].

9.4.1 Generalized Rytov variance

To illustrate the approach required for the more general anisotropic spectrum model [Eq. (9.44)] extended over all wavenumbers, we again start with the generalized Rytov variance in homogeneous turbulence at range L, defined by

$$\begin{aligned}\tilde{\sigma}_R^2(\alpha, \mu_x, \mu_y) &= 4\pi k^2 L \int_0^1 \int_{-\infty}^{\infty} \int_{-\infty}^{\infty} \Phi_n(\kappa_x, \kappa_y, 0)\left[1 - \cos\left(\frac{L\kappa^2\xi}{k}\right)\right] \\ &\quad \times d\kappa_x d\kappa_y d\xi \\ &= 4\pi k^2 L \int_0^{2\pi} \int_0^1 \int_0^{\infty} q\Phi_n(q, 0) \\ &\quad \times \left\{1 - \cos\left[\frac{Lq^2\xi}{k}\left(\frac{\cos^2\theta}{\mu_x^2} + \frac{\sin^2\theta}{\mu_y^2}\right)\right]\right\} \frac{dq d\xi d\theta}{\mu_x \mu_y},\end{aligned} \tag{9.56}$$

where $\xi = 1 - z/L$ and $\kappa^2 = \kappa_x^2 + \kappa_y^2$. In the second step above we changed from a stretched coordinate system for the spectrum to one that is isotropic through the substitutions

Chapter 10
Measuring Optical Turbulence Parameters

10.0 Introduction

In this chapter we discuss the use of various instruments that infer or measure atmospheric parameters like the refractive-index structure parameter, inner scale, temperature, wind speed, heat flux, and so forth. Of course, the conventional instruments that researchers use are all based on the assumption of isotropic, Kolmogorov turbulence. Although we know that anisotropic conditions and non-Kolmogorov turbulence may sometimes exist in the lower atmosphere (see Chapter 9), we do not take that into account in our treatment here.

Turbulence parameters such as C_n^2 can be determined either by direct measurement of turbulence or by its effect on propagated light. It would be ideal to characterize turbulence along the path by directly measuring fluctuations in the refractive index. However, with current technology, the closest that we can come to measuring refractive-index fluctuations is to measure temperature fluctuations, and from these measurements calculate the corresponding refractive-index fluctuations. (This value can be improved by including humidity effects.) These are small volume or near-point measurements of temperature and are only valid at the location of the measurement itself. The alternative is to propagate light through the atmospheric turbulence in the form of a light-emitting diode (LED) or laser and measure the resultant effect on the light, such as scintillation or jitter, which can then be related to turbulence parameters through propagation theory. However, depending on the optical method chosen, the resultant turbulence parameters are generally path-averaged, with each method having a corresponding weighting function. For instance, assuming spherical-wave propagation, a scintillation-based method is weighted toward the center of the path, whereas a method based on image motion is weighted toward the receiver (Rx).

In the following sections, we consider common methods of determining atmospheric turbulence parameters. This discussion is divided into methods

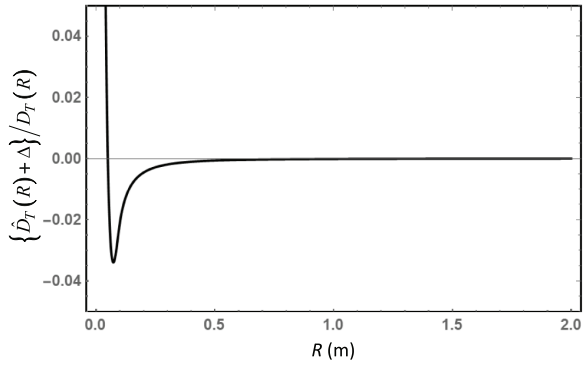

Figure 10.5 Relative error resulting from adding constant offset to a line-averaged structure function for Kolmogorov turbulence.

Fig. 10.1, which demonstrates the deviation of the structure function from theory at the outer scale. In practice, it may be easier to work with

$$\log[D_T(R)] = \frac{2}{3} C_T^2 \log(R) \tag{10.26}$$

and find where the slope of this linear curve changes at the outer scale.

10.2 Turbulence Inference Based on Optical Measurements

As an alternative to direct turbulence measurements, one can measure the impact that the turbulence has on light that has propagated through it and compare this to the theoretically predicted effect based on the wavelength and path length as a function of C_n^2.

10.2.1 Image motion measurement

Fluctuations in phase due to refractive index variations result in fluctuations in angle-of-arrival or image motion, also known as jitter. Image motion can be related to theory to infer C_n^2. However, this method is sensitive to all motion (e.g., vibration) so, in practice, *differential image motion measurement* (DIMM) is more commonly used as it removes any motion common to both Rxs, generally making it more robust. In this section we discuss the equations describing image motion, and in Section 10.2.1.1 we extend this to the more mathematically complicated DIMM or tilt anisoplanatism.

Figure 10.6 shows the configuration that corresponds to this mathematical analysis where we consider the phase difference from a single source propagating over a path length L as seen from two displaced locations separated by a distance d. The analysis could similarly be performed for two Txs and a single Rx.

strong extended-turbulence atmospheric paths. The acquired tilt data is processed to estimate the DDTV quantities, which are unaffected by gimbal motion and additive noise sources.

The DDTV quantities each represent a particular weighted integral of C_n^2 over the propagation path. By using the theoretical weighting function for the DDTV measurements, a reconstructor matrix can be derived to obtain C_n^2 estimates over the entire propagation path. These weighting functions are independent of the actual turbulence profile and depend only on the geometry of the apertures and the sources for the profiler hardware.

The DDTV technique can be implemented in either a passive or active configuration. Using a camera and image processing, pairs of features can be tracked, and differential jitter can be measured between them as a function of angular separation. A turbulence profile is generated by applying the DDTV method to this data. An active implementation requires two Rx apertures and a focal plane camera at one end of the path and three-point source beacons at the other end. The apertures can be used to observe either a single point source (such as the aperture used in a DIMM system as discussed in Section 10.2.1.2) or two individual point sources (like the point source discussed in Section 10.2.1.3).

Appendix 10A

Comparisons of Multi-Source Tilt Anisoplanatism Models

Shown in Fig. 10A.1 are some graphical comparisons of the different multi-source tilt anisoplanatism models defined by Eqs. (10.56) through (10.59). Equations (10.56) and (10.57) are exact expressions based on the relation given in Eq. (10.52), which is known to be an accurate approximation to the filter function.[17] We plot two cases for $\sigma^2_{LED\perp}$ and $\sigma^2_{LED\parallel}$, corresponding to the Rx aperture diameters $D = 0.05$ m and $D = 0.1$ m, respectively, both as a function of source separation d.

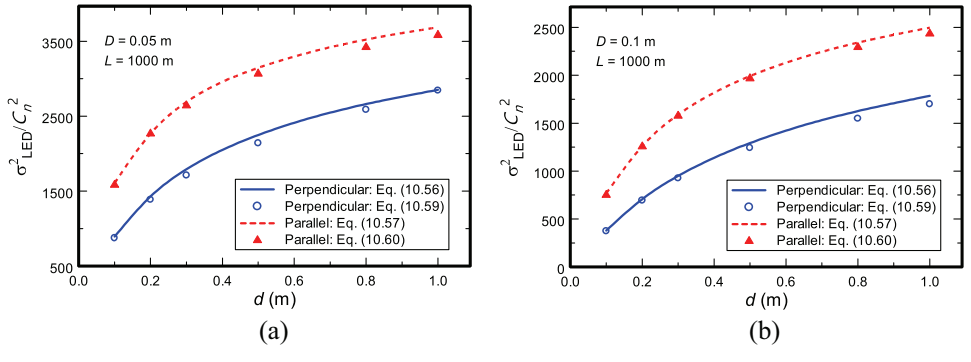

Figure 10A.1 Tilt anisoplanatism plots for (a) $D = 0.05$ m and (b) $D = 0.1$ m.

Larry C. Andrews is Professor Emeritus of Mathematics at the University of Central Florida and an associate member of the Townes Laser Institute in the College of Optics/CREOL. He previously was also an associate member of the Florida Space Institute (FSI) and had a joint faculty appointment with the Department of Electrical and Computer Engineering. Before that, he held a faculty position at Tri-State University and was a staff mathematician with the Magnavox Company, antisubmarine warfare (ASW) operation. He received a doctoral degree in theoretical mechanics in 1970 from Michigan State University. Dr. Andrews has been an active researcher in optical wave propagation through random media for more than 35 years and is the author or co-author of twelve textbooks on topics of differential equations, boundary value problems, special functions, integral transforms, wave propagation through random media, and mathematical techniques for engineers. He is a Fellow of SPIE and the author of three *Field Guides* on Atmospheric Optics, Special Functions, and Random Processes. Along with wave propagation through random media, his research interests include special functions, random variables, atmospheric turbulence, and signal processing.

Melissa K. Beason has a diverse research background spanning more than 20 years that includes laser sources, acoustics, and atmospheric propagation. She is currently an Assistant Research Professor with the Air Force Institute of Technology. She received her Ph.D. in Electrical Engineering from the University of Central Florida (UCF) in 2018. Prior degrees include a Master of Science Degree in Mathematical Sciences from UCF and a Bachelor of Science Degree in Physics from the University of Florida. Dr. Beason also held Research Physicist positions with the Air Force Research Laboratory, Directed Energy Directorate and the Naval Research Laboratory, Underwater Sound Reference Detachment. She was a Preeminent Postdoctoral Scholar with UCF and European Research Consortium in Informatics and Mathematics Fellow during which she collaborated with the Adaptive Optics Group of the Fraunhofer Institute of Optronics, System Technologies and Image Exploitation IOSB. Dr. Beason's research interests include atmospheric propagation through random media and turbulence measurement.